



**HAL**  
open science

# Experimental investigation of the delayed behaviour of unsaturated argillaceous rocks by means of Digital Image Correlation techniques

Diansen Yang, Michel Bornert, Serge Chanchole, Linlin Wang, Pierre Valli, Behrouz Gatmiri

► **To cite this version:**

Diansen Yang, Michel Bornert, Serge Chanchole, Linlin Wang, Pierre Valli, et al.. Experimental investigation of the delayed behaviour of unsaturated argillaceous rocks by means of Digital Image Correlation techniques. *Applied Clay Science*, 2011, 54 (1), pp.53-62. 10.1016/j.clay.2011.07.012 . hal-00682470

**HAL Id: hal-00682470**

**<https://enpc.hal.science/hal-00682470>**

Submitted on 25 Apr 2022

**HAL** is a multi-disciplinary open access archive for the deposit and dissemination of scientific research documents, whether they are published or not. The documents may come from teaching and research institutions in France or abroad, or from public or private research centers.

L'archive ouverte pluridisciplinaire **HAL**, est destinée au dépôt et à la diffusion de documents scientifiques de niveau recherche, publiés ou non, émanant des établissements d'enseignement et de recherche français ou étrangers, des laboratoires publics ou privés.



Distributed under a Creative Commons Attribution - NonCommercial 4.0 International License

# Experimental investigation of the delayed behavior of unsaturated argillaceous rocks by means of Digital Image Correlation techniques

Diansen Yang <sup>a,\*</sup>, Michel Bornert <sup>b</sup>, Serge Chanchole <sup>a</sup>, Linlin Wang <sup>a</sup>, Pierre Valli <sup>a</sup>, Behrouz Gatmiri <sup>c</sup>

<sup>a</sup> *Laboratoire de Mécanique des Solides, École Polytechnique, 91128 Palaiseau, France*

<sup>b</sup> *Laboratoire Navier, Université Paris-Est, École des ponts ParisTech, Champs-sur-Marne, 77544 Marne-la-Vallée, France*

<sup>c</sup> *Agence nationale pour la gestion des déchets radioactifs (ANDRA), 92298 Châtenay-Malabry, Cedex, France*

We present an experimental study on the delayed behavior of unsaturated argillaceous rocks, including shrinkage, swelling, and creep, by means of Digital Image Correlation (DIC) techniques. In order to measure the very low strain rate of the argillaceous rocks at various scales (100  $\mu\text{m}$ –cm) under uniaxial compression and various environmental conditions, a specific optimized optical setup was used. The natural argillaceous rocks were hydrated or dehydrated by controlling the ambient humidity around the samples, and the obtained unsaturated samples were then subjected to creep tests at different stress levels. The mechanical response to hydration and dehydration strongly depended on the mechanical loading, which induced an additional deformation. During creep, the strain rate increased when the moisture or the applied stress increased. The strain rate at a relative humidity of 75% was about one order of magnitude larger than at a dried state (relative humidity = 25%). The anisotropy of the strain induced by the moisture and mechanical loading was enhanced over time. The time dependent behavior as observed at different scales (100  $\mu\text{m}$ –cm) is discussed.

## 1. Introduction

In France, the argillaceous formation at the depth of 500 m in the site of Meuse/Haute Marne (MHM) is considered as a potential host rock for high level radioactive nuclear waste repository because it presents several favorable properties, such as very low permeability ( $<10^{-21} \text{ m}^2$ ), relative homogeneity of the mechanical behavior, etc. (Yang et al., 2010a,b). In order to reasonably estimate the operability and the safety of the underground nuclear waste repository over a long time, one needs a deeper understanding of the delayed behavior, including swelling and creep under different conditions (moisture, stress, temperature), in order to estimate the time-dependent displacements of the host rocks during the repository life (Bérest, 1987; Fabre and Pellet, 2006; Gasc-Barbier et al., 2004; Pusch, 1993; Shao et al., 2003).

The behavior of the MHM argillaceous rocks was strongly dependent on the water content (Pham et al., 2007; Valès, 2008; Yang et al., 2010a; Zhang et al., 2007). For instance, the peak strength increased from 15 MPa to 45 MPa and the Young's modulus increased from 5 GPa to 12 GPa when the water content decreased from 8.6% to 3.0% (Valès, 2008), and the effective gas permeability increased

during dehydration (Yang et al., 2010a). The microstructures of clayey materials changed during hydration and dehydration which induced swelling or shrinking. Such studies mainly reported the hydration and dehydration effects under stress free condition.

In addition to the water content, the mineralogical composition and the microstructure could play an important role in the propagation of damage of the argillaceous rocks (Gasc-Barbier et al., 2004; Wright, 2002).

The delayed deformation is also strongly related to the extrinsic parameters (deviatoric stress, temperature): a higher deviatoric stress could induce a larger viscoplastic strain, material rupture and increased permeability (Shao et al., 2003; Yang et al., 2010a; Zhang et al., 2007) and the rate and the range of deformation have been observed to increase with temperature (Gasc-Barbier et al., 2004). In this study, the effect of temperature on the delayed strain was not considered.

Given that the heterogeneous argillaceous rocks at microscale ( $\mu\text{m}$ ) present a possible very slow strain rate, e.g.  $10^{-11} \text{ s}^{-1}$  (Gasc-Barbier et al., 2004), we developed an optimized optical setup to determine the full field strain of the material and studied the time dependent deformation of the argillaceous rock under combined moisture and mechanical loading. This setup combines a coupled moisture and stress control with an optical observation at both the centimetric scale of the sample and the near micrometric scale of its microstructure, in line of the one used by Bornert et al. (2010). Its main features are roughly discussed in Section 3. Additional technical details on the optimization of its performances are given elsewhere (Yang et al., 2010b).

\* Corresponding author.

E-mail address: yang@lms.polytechnique.fr (D. Yang).

## 2. Material

The MHM argillaceous rock is a complex material and contains an average of 40–45% clay minerals, 22–37% carbonates, 25–30% quartz and <5% of other materials (for example, pyrite). The SEM observation of the core plug EST28031 taken from the site MHM at the depth of 553 m showed that the size of the carbonate and quartz grains varied from a few micrometers to a few hundred micrometers (Fig. 1). They were scattered in a clay matrix with a particle size in the submicrometric range. In a similar material, the porosity of the material was about 15%, the pore sizes varied between 20 nm and 50 nm, occupying about 50% of the Hg porosity (Yang et al., 2010a). Such pore size distribution led to very low permeability. The particle density of the material was estimated as  $2.72 \text{ g/cm}^3$  and the apparent density of the material was about  $2.40 \text{ g/cm}^3$  at natural state.

The initial water content of the MHM argillaceous rocks varied between 5% and 9%. The water was mainly contained in the clay matrix. The initial water content of the core plug EST28031 was estimated as 6.3% by oven-drying several reference samples until the weight remained constant. The variation of the water content during hydration or dehydration can change the microstructure of the material and influences the mechanical properties.

Due to the layered morphology of the clay mineral and because of the rock formation processes, the mechanical properties of the argillaceous rock are strongly anisotropic. This anisotropy can be generally well described by transverse isotropy and can be modeled from the clay-particle orientation distribution (Sayers, 1994). Niandou et al. (1997) and Valès et al. (2004) showed that the compression strength depended on the angle  $\theta$  between the applied stress direction and the stratification plane and presented a nearly linear dependence with  $\theta$  when the latter varied between  $45^\circ$  and  $90^\circ$ , but this relation no longer held for  $\theta=0$ . The study of Fabre and Pellet (2006) on the argillaceous rock also confirmed that the elastic modulus and compression strength depended on the orientation of the sample. An interpretation of this observation was that the anisotropic behavior would result from interactions between matrix and joints deformations, which depend on the loading orientation (Fabre and Pellet, 2006). Under moisture and mechanical loading, this natural anisotropy of the material can be changed because of the microstructure changes.

## 3. Methods

### 3.1. Methods

Due to several favorable properties, such as noncontact and full-field measurement, Digital Image Correlation techniques are widely

used to investigate the mechanical properties of structural materials such as metals, polymers and composites (Sutton et al., 2009). DIC technique uses a specific correlation algorithm to compare two images acquired by a CCD camera at different states (Chu et al., 1985; Sutton et al., 1983) in order to identify corresponding subsets in the two images. When the correlation between the reference image and the deformed image subsets is minimized, which indicates optimal matching, the local displacements can be calculated by comparing the center point position of each subset. The local strain field as well as its averages over various domains of interest can be then determined by the discrete differentiation procedure described in Allais et al. (1994) and Bornert et al. (2010).

However, this method is seldom used in rock mechanics because such materials present very low strain levels before failure, especially when creep is considered. For instance, the typical strain rate of argillaceous rock in creep tests is about  $10^{-11} \text{ s}^{-1}$ , i.e. about  $10^{-5}$  per week (Gasc-Barbier et al., 2004; Pham, 2007). To determine local full-field strain and to study the time dependent changes of the microstructure, the strain must be measured with an accuracy better than  $10^{-5}$  over long time periods, not only at the macroscopic scale of the centimetric sample but also at the local scales at which creep mechanisms are suspected to act.

### 3.2. Equipment

A specific optical setup was designed and developed at the LMS (Solid Mechanics Laboratory, Ecole Polytechnique) (Bornert et al., 2010; Yang et al., 2010b) to apply the DIC technique to the uniaxial compression test. This system mainly consisted of the following parts: macroscopic and microscopic optical setups; mechanical loading device; and suction control equipment.

The macroscopic optical setup (MacroDIC) observed an area of  $24 \times 36 \text{ mm}$  with the magnification of 1, and each square pixel of the 16 MP image was  $7.4 \mu\text{m}$  in width. The MacroDIC was fixed during the test. The observed object area of the microscopic optical setup (MicroDIC) was  $1.5 \times 1.5 \text{ mm}$  and the pixel size was  $0.74 \mu\text{m}$ . The microscopic camera was mounted on a servo-controlled micrometric X–Y–Z translation stage. With this servo-control, the Z position (normal to the sample) was automatically adjusted for sharp focus by means of a contrast maximization algorithm (Yang et al., 2010b). The camera can be moved automatically along X and Y directions to observe several juxtaposed zones and center them on positions of interest by means of standard DIC algorithms. The MicroDIC setup was opposite with the MacroDIC setup. Because of the low depth of field of both optical systems, the cylindrical samples had to be flattened symmetrically.

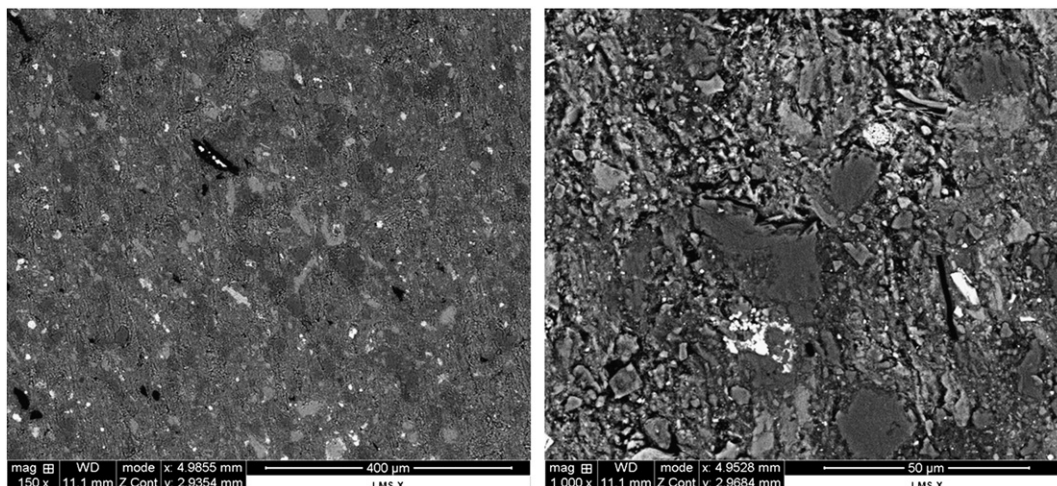


Fig. 1. Microstructure of the argillaceous rocks (sample of EST28031-A).

The force was applied by a rigid electromechanical machine. Both force and displacement control can be used. The force can be increased to 100 kN and the controlled speed of the crossbeam displacement can be as low as 1  $\mu\text{m/s}$ .

The suction has been imposed by means of supersaturated saline solutions (Delage et al., 1998) which were placed near the sample inside an airtight PMMA container, about  $25 \times 25 \times 40$  cm in size, in which holes have been machined for the optics and the loading line and carefully tightened to limit the gas exchanges to a minimum.

Several specific procedures have been proposed to control and improve the measurements accuracy and to correct the errors induced by the overall micrometric out-of-plane motion of the sample on the macroscopic DIC measurements (Yang et al., 2010b). With these improvements, the current optimized optical setup ensures an accuracy better than  $10^{-5}$  at the sample scale (cm) and  $>10^{-4}$  at the local scale (100  $\mu\text{m}$  gage length).

### 3.3. Procedure

#### 3.3.1. Sample and surface preparation

Several cylindrical samples with a diameter of 36 mm and a height of about 36 mm have been machined from the core plug EST28031 and EST28036. Their axis was perpendicular to the bedding plane ( $\theta = 90^\circ$ ). The flat surfaces with a width of about 24 mm were dry polished to grade 4000, one facing the macroscopic camera and the other facing the microscopic camera. The MacroDIC observed the total surface area ( $24 \times 36$  mm) and the MicroDIC observed 4 local zones ( $1.5 \times 1.5$  mm), which were chosen in the central zone of the whole surface.

#### 3.3.2. Application of the moisture and mechanical loading

The prepared samples were placed in an airtight container, and a cycle of loading and unloading was applied on the ends of the sample by controlling the speed of displacement at 1  $\mu\text{m/s}$  to determine the mechanical properties of the argillaceous rocks at its initial state. The samples were then hydrated or dehydrated by changing the moisture, which was controlled by the supersaturated saline solution. When the sample reached the equilibrium, the axial stress was increased to a defined level and kept constant for several weeks until the steady state was reached where the strain rate was considered constant. Then, the stress was increased for another creep test. In this study, the two samples (EST28031-A and EST28031-B) were equilibrated at the humidity of 65% and 80%. The creep tests were done at three stresses (9 MPa, 14 MPa, and 18 MPa). Each creep test lasted about 2 weeks (Fig. 2a). In order to evaluate the effect of the moisture history, two tests were performed on the sample EST28031-C and EST28036-A machined from the core plug EST28036 taken at the depth of 555 m. EST28031-C was firstly dehydrated at the humidity of 25% for 4 successive creep tests at the stresses (10 MPa, 16 MPa, 20 MPa, and 10 MPa), then hydrated at the humidity of 75% for the other two creep tests at 10 MPa and 20 MPa. EST28036-A was firstly hydrated at the humidity of 75% before two creep tests were performed at 13 MPa and 18 MPa. This sample was finally dehydrated at the humidity of 40% at the steady state of the creep test at 18 MPa. Because of power failure this test was limited at 4 MPa (Fig. 2b). The two tests lasted more than 3 months.

#### 3.3.3. Characterization of heterogeneity in the material

Four juxtaposed zones of interest ( $1.5 \times 1.5$  mm) have been observed with MicroDIC during testing. The zone may be a cracked zone as the case of EST28031-A (Fig. 3c) or an intact zone as 4 zones of EST28031-B (Fig. 3b,d). The heterogeneity of the material at the mesoscopic scale was analyzed by comparing the gray level of the images, which was obtained under the orthodromic lighting at the beginning of the test, and counting the bright subset area which was considered to represent the grains (e.g. carbonates). The estimated grains consisted of about 35%

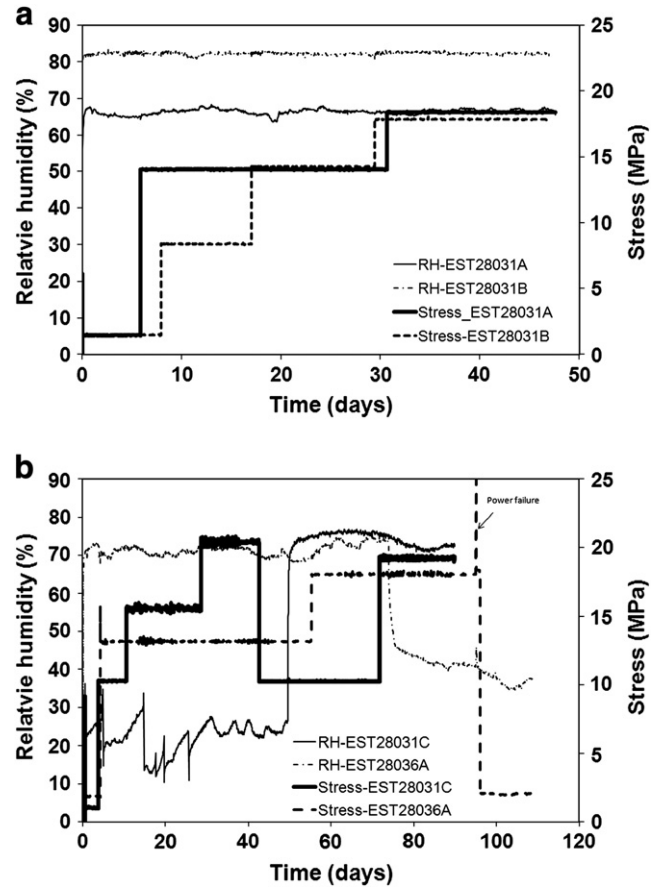


Fig. 2. The moisture-mechanical loading paths of the samples (a: EST28031-A,B; b: EST28031-C, EST28036-A).

of the material (Table 3) and only 30% in zone 4 (Fig. 3d). Such heterogeneous composition could cause the different response of the material subjected to the moisture and mechanical loading. In order to study the heterogeneity of each mineral particle, which was homogeneous under the orthodromic lighting, the images were captured under the slide lighting during the test.

In order to study the heterogeneous behavior of the material at different states, all the images captured by the two cameras were analyzed by the use of the DIC technique presented above (Section 3.1) to obtain the full-field strain. The whole flat surface ( $24 \times 36$  mm), several local zones (a few millimeters) in the macroscopic images (e.g. Zone-A in Fig. 3a), the whole zone of the microscopic images ( $1.5 \times 1.5$  mm) and several local zones (100  $\mu\text{m}$ ) with clay minerals or grains (Fig. 3b) were chosen to investigate the behavior at various scales. In the next part, the macroscopic strain means the average strain over the whole surface and the mesoscopic strain means the average deformation in millimeter. The positive value of the strain at the strain curve represented contraction and the negative one dilatation.

Note that images were recorded every 3 s during the initial loading cycle, and when the stress was modified, in order to quantify the instantaneous response of the samples. During creep test, the image recording rate was reduced to one image every 30 min. Altogether these tests generated more than 1 Terabytes of data.

## 4. Results

### 4.1. Mechanical properties at initial state

The first loading and unloading cycle was done by increasing the stress from 0 MPa to 6 MPa and then reducing it to 1 MPa. The

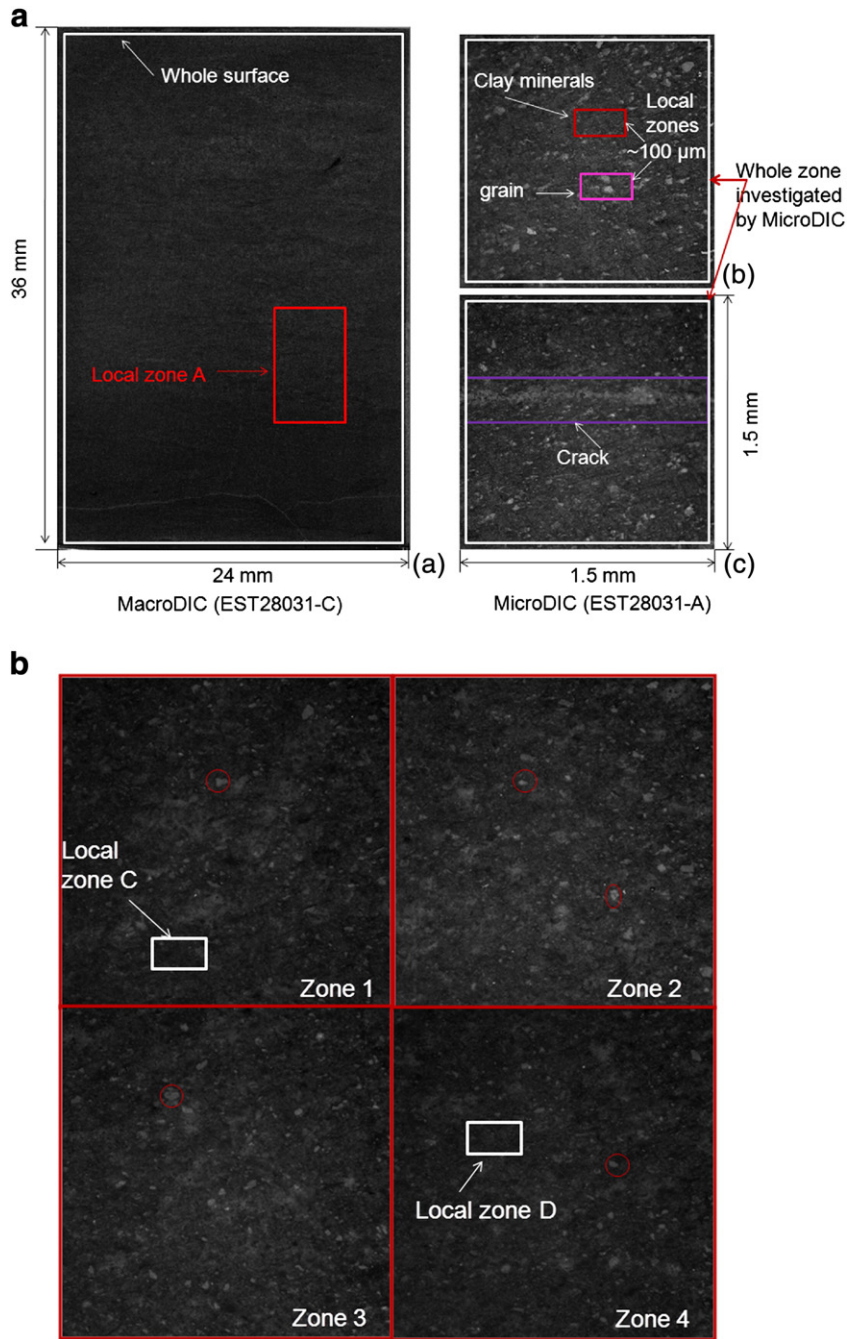


**Fig. 3.** Investigated scales by MacroDIC and MicroDIC(a: whole surface and local zone observed by MacroDIC; b, c, d: intact zone/cracked zone and local zones observed by the MicroDIC).

obtained unloading part of the stress strain curve at the macroscopic scale (cm) (Fig. 5a) was used to determine the elastic properties (Young's modulus  $E$  and Poisson's ratio  $\nu$ ) of the samples at their initial states (Table 1). EST28031-C ( $E = 8.7$  GPa) at initial state was more rigid than EST280031-A ( $E = 4.7$  GPa), EST280031-B ( $E = 6.5$  GPa), and EST28036-A ( $E = 5.0$  GPa). These differences in moduli should be mainly related to the different water contents because the samples were not tested immediately after the preparation. For instance, EST280031-A was first tested and EST280031-C was tested at last. EST280031-B and EST280031-C had a lower water content compared to EST280031-A. Assuming that the initial water content of the core plug corresponds to a relative humidity above 85% (Valès, 2008), the low water content of EST28031-B at the initial state can also explain why it hydrated at the humidity of 80% and

EST28031-C contracted only very moderately at the humidity of 25% (Section 4.2). The Poisson coefficient was about 0.15 for all these samples. It confirmed that the Poisson's coefficient was almost insensitive to relative humidity during hydration and dehydration cycles (Yang et al., 2010b).

#### 4.2. Swelling and shrinking

Because of the different initial water contents, EST28031-A and EST28031-C were dehydrated under the controlled moisture conditions ( $RH = 65\%$  and  $RH = 25\%$ ) and EST28031-B and EST28036-A were hydrated at the humidity of 80% and 75%. The equilibrium, detected from the stabilization of the strains measured by DIC, was reached after 1 week. The characteristic time for this sample size is

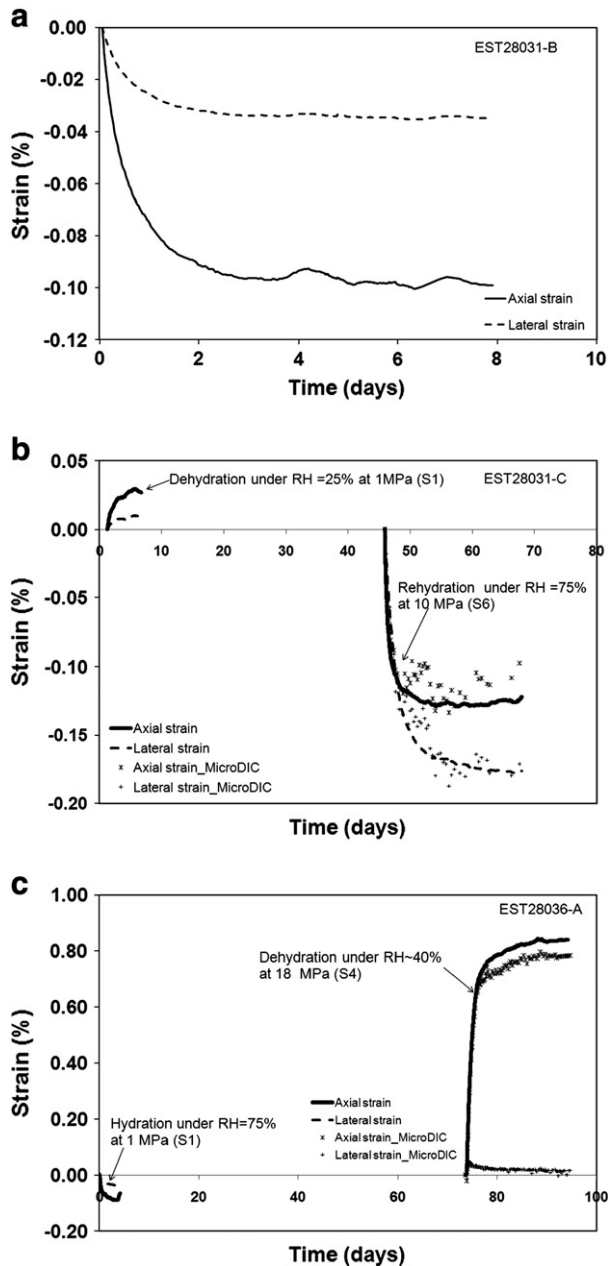


Fig. 4. Strain-time curve of the sample EST28031-B (a) during hydration, EST28031-C (b) and EST28036-A (c) during dehydration and rehydration.

comparable to that obtained in an earlier study (Valès, 2008) and corresponds to a diffusion coefficient of about  $10^{-10}$  m/s, as evaluated by a numerical study (Yang et al., 2010a).

The linear relation between the water content and the relative humidity allowed to estimate the water content of the samples at the moisture equilibrium (Yang et al., 2010a). For instance, EST28031-B had a water content of 5.8% when it reached the equilibrium and EST28031-C 2.1% at the humidity of 25% and 5.5% at the humidity of 75%. EST28036-A had a water content of 5.5% at the humidity of 75% and of 3.7% at the humidity of 40% (Table 2). These water contents were lower than the initial water content of the core plug (6.3%). Thus, dehydration of the sample during the sample preparation and conservation was confirmed.

The strain-time curves showed that EST28031-B and EST28036-A swelled during hydration (Fig. 4a,c) while EST28031-A and EST28031-C contracted during dehydration (Figs. 5a and 4b) in the first period. As long as the moisture content does not exceed a

threshold value, the capillary pressure is dominant and the material deformed nearly linearly as a function of the humidity or the water content (Valès, 2008; Yang et al., 2010a).

The ratio between the lateral strain in the direction parallel to the bedding plane and the axial strain in the direction perpendicular to the bedding plane provides a measure of the anisotropy of the swelling/shrinking behavior of the rock. This anisotropy was related to the foliated structure of the clay minerals and the rock formation processes. The ratio was about 0.3 at 1 MPa. But for the complex tests, it varied much at higher stress (10 MPa and 18 MPa) (Fig. 4b,c). The lateral swelling of EST28031-C ( $-0.18\%$ ) was larger than the axial one ( $-0.13\%$ ) when increasing the relative humidity from 25% to 75% at 10 MPa. For EST28036-A, the lateral shrinkage (0.04%) was much less than the axial strain (0.83%) at 18 MPa when the humidity decreased from 75% to 40%. While the deformation of the argillaceous rocks induced by the variation of the relative humidity was about  $10^{-4}$  per RH degree under stress free conditions (Yang et al., 2010b), the obtained deformation at high stress seemed to follow more complex laws, probably related to other phenomena like creep, the heterogeneous stress distribution during hydration and dehydration, the effect of mechanical loading, the anisotropy induced during the tests, or damage. As the largest measured strain rate was below  $10^{-9}$  s $^{-1}$  at 18 MPa for EST28036-A, the increase of the axial strain due to creep would be below  $10^{-4}$  per day. Thus, the creep behavior can not be the principal reason for the large deformation (e.g. 0.83%) observed during RH changes. The moisture transfer of the argillaceous rocks was a long process and it needs about 1 week to reach a homogeneous distribution of the water in the sample. Thus, it can induce a heterogeneous stress distribution in transient periods (Jia et al., 2010). The heterogeneous stress may lead to a heterogeneous deformation. Also, as shown in Fig. 4b and c, the strain measurements at the macroscopic scale (cm) is very close to those at one local zone (mm) of the sample. The local zone should be less affected by the heterogeneous stress. The applied stress can restrain the swelling and influence the deformation. This induced the contraction in axial direction and the extension in lateral direction. It could be the principal reason for the increase of the lateral dilatancy during hydration and the small contraction during dehydration at high stresses. This suggested that swelling/shrinking was a physical phenomenon strongly dependent on the applied stress, which cannot be described by classical linear hydromechanical constitutive relations.

#### 4.3. Creep behavior at the macroscopic scale (cm)

When the moisture equilibrium was reached, the creep tests were conducted at different stress levels. Fig. 5a,b,c, and d respectively presents the strain at the macroscopic scale (cm) determined from the whole surface of the sample and the stress/humidity history curves of these four samples. All the creep tests apparently presented two phases: the primary creep phase, during which the strain rate decreased, and the secondary steady phase with a constant strain rate, except for the last creep test of EST28031-C, which exhibited in addition a tertiary phase in the last creep test at 20 MPa just before failure (Fig. 9). To easily present different creep tests, all the steps are named in Fig. 5. For instance, the creep test of EST28031-A at 14 MPa was named as S2 (Fig. 5a).

The measurements were disturbed by the variation of the relative humidity, which was not always constant. Such variation was large and can hide the creep behavior subjected to the mechanical loading. The strain of this material induced by the variation of the relative humidity was about  $10^{-4}$  per RH degree under unconfined condition. It was a quasi-linear function of the relative humidity when the later was  $<85\%$  (Yang et al., 2010a, 2010b). Considering the delayed response of the material subjected to the moisture loading, a simple formula was proposed to correct the strain measurement:

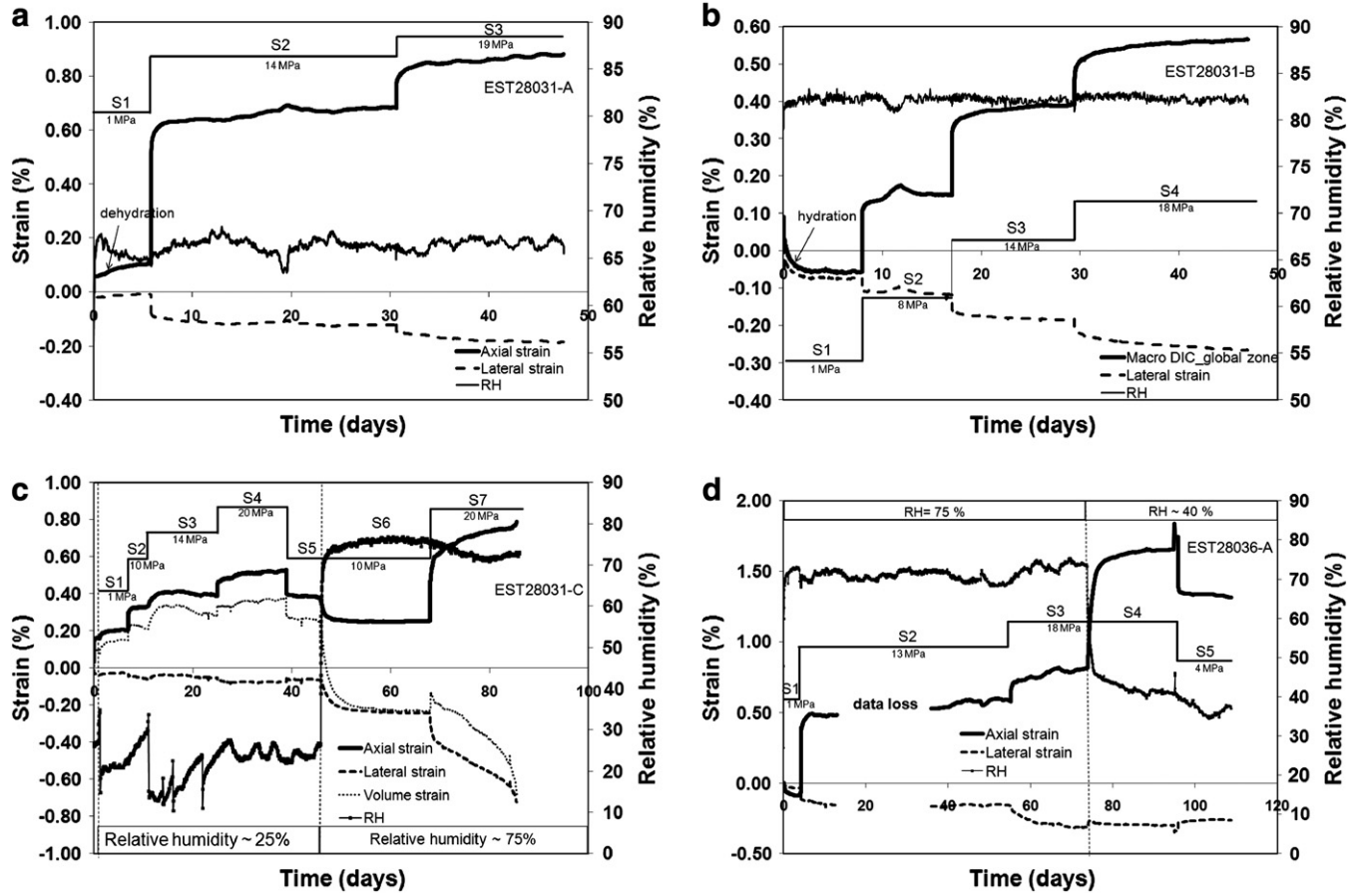


Fig. 5. Strain curve at the macroscopic scale MacroDIC (cm) during the creep test (a: EST28031-A; b: EST28031-B; c: EST28031-C; d: EST28036-A) (volume strain  $\varepsilon_v = \varepsilon_1 + 2\varepsilon_2$ ).

$\varepsilon^{\text{correct}}(t) = \varepsilon^{\text{real}}(t) - b \cdot \Delta RH(t - \Delta t)$ , where  $t$  is real time and  $\Delta t$  is characteristic time (the delayed response of the hydration, 2 h),  $\Delta RH(t)$  is the variation of the relative humidity at time  $t$  with respect to the RH at which the sample reached the moisture equilibrium and  $b$  is the coefficient of the linear function between the strain and the relative humidity ( $10^{-4}$ ). This formula was used to correct the deformation of EST28031-A and the strain rate was determined from the corrected strain curves (Fig. 6). This correction can only be used when the relative humidity variation is small.

In fact, the strain rate did not reach a constant rate at the end of each step, even if the creep test lasted more than 2 weeks (Fig. 7). For EST28031-A, it decreased from  $3 \times 10^{-10} \text{ s}^{-1}$  (15th–20th day) to  $4 \times 10^{-11} \text{ s}^{-1}$  (26th–30th day) at 14 MPa. By considering the disturbance related to the humidity and the realistic test time, each creep test was done about 2 weeks. The strain rates of the sample were determined from the strain curves in the last four days of each creep step and they are presented in Table 2. The axial strain rates varied between  $10^{-9} \text{ s}^{-1}$  and  $10^{-11} \text{ s}^{-1}$ . They generally increased with stress level and moisture level.

Because the strain rate of EST28031-C at 10 MPa and 14 MPa at dried state was very low ( $< 10^{-11} \text{ s}^{-1}$ ), the measurements were disturbed by

**Table 1**  
Mechanical parameters (Young's modulus and Poisson's ratio) at initial state.

Sample	Diameter (mm)	Length (mm)	Width (mm)	E (GPa)	$\nu$
EST28031-A	36.0	36.0	25.2	4.6	0.15
EST28031-B	36.0	36.0	26.0	6.5	0.16
EST28031-C	36.0	36.4	25.1	8.7	0.16
EST28036-A	36.0	36.0	25.0	5.1	0.15

humidity changes. We could not determine precisely the strain rate for these two steps. The axial strain rate was  $1.42 \times 10^{-10} \text{ s}^{-1}$  at 20 MPa. At the humidity of 75%, the axial strain rate increased from  $2.5 \times 10^{-11} \text{ s}^{-1}$  at 10 MPa to  $1.2 \times 10^{-9} \text{ s}^{-1}$  at 20 MPa and the lateral strain rate increased rapidly from  $-2.4 \times 10^{-11} \text{ s}^{-1}$  at 10 MPa to  $-2.1 \times 10^{-9} \text{ s}^{-1}$  at 20 MPa. This large variation was related to the fact that the crack developed during testing (Section 4.5). To study the irreversible strain during the creep test and also to avoid the possible rupture of the sample during hydration for the next creep tests, the axial stress was decreased from 20 MPa to 10 MPa, which was kept constant about 1 week before the changes in the humidity. During this period, the inverse creep was found and the sample continued to dilate. The irreversible axial strain was about 0.06% and the irreversible lateral strain about  $-0.01\%$ .

For EST28036-A the axial strain rate at 18 MPa decreased from  $1.7 \times 10^{-9} \text{ s}^{-1}$  to  $6.9 \times 10^{-10} \text{ s}^{-1}$  when the relative humidity

**Table 2**  
Axial strain rate at the macroscopic scale (centimetric gage length) during the last 4 days of each creep test.

Sample	RH	W	Step	$\varepsilon^{\text{axial}}$ ( $\times 10^{-11} \text{ s}^{-1}$ )
EST28031-A	65%	4.8%	S2	4
			S3	25
EST28031-B	80%	5.8%	S2	1
			S3	5
			S4	27
			S7	122
EST28031-C	25%	2.1%	S4	14
	75%	5.5%	S6	3
EST28031-A	75%	5.4%	S2	49
			S3	170
EST28036-A	40%	3.7%	S4	69

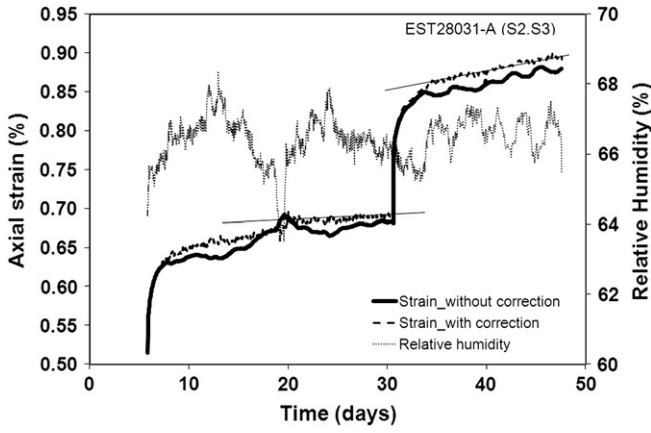


Fig. 6. Correction of strain disturbed by the variation of the relative humidity.

decreased from 75% to 40%. The strain rate of this sample was relatively larger than for EST28031-A and -B (Table 2). The difference was mainly related to the mineralogical composition. The core plug EST28031 had a higher carbonate content (35%). The results of the two complex tests showed that the hydration/dehydration cycles can influence significantly the strain rate, and even lead to the rupture of the sample.

#### 4.4. Creep behavior at the mesoscopic scale

The strain curves of the 4 zones in millimeters with different grain contents of EST28031-B (Fig. 8a) showed that they had similar behavior and they were consistent with those obtained at macroscopic scale (cm). The small difference of the strain and the strain rate among these zones can be mainly related to the heterogeneous composition at the considered scale (mm) (Table 3). For instance, zone 4 and zone 1 deformed more than zone 2, not only during mechanical loading, but also during hydration, because zone 4 and zone 1 had a larger amount of clay minerals.

The heterogeneous behavior related to the mineralogical composition is very clear in Fig. 8b, which showed that the strain obtained at 100  $\mu\text{m}$  of the local zone C with clay minerals in the zone 1 was larger than that at the mesoscopic scale (mm), moreover it was more sensible to the changes in the humidity relative than the zone 1. Even if the humidity varied in the range of 1%, the obtained strain changed about 0.1%. Such variation was much larger than the creep behavior subjected to the mechanical behavior. So it is difficult to determine the strain rate at 100  $\mu\text{m}$  with the actual MicroDIC setup. Some improvements of the optical MicroDIC and the humidity control are ongoing to try to minimize the noise and obtain the best resolution at the microscale (100  $\mu\text{m}$ ).

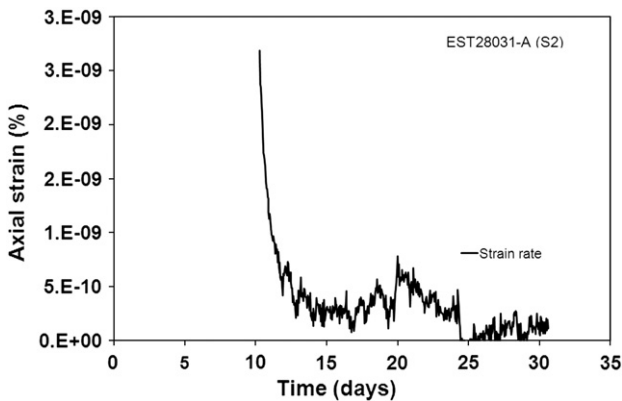


Fig. 7. Axial strain rate of EST28031-A at 14 MPa.

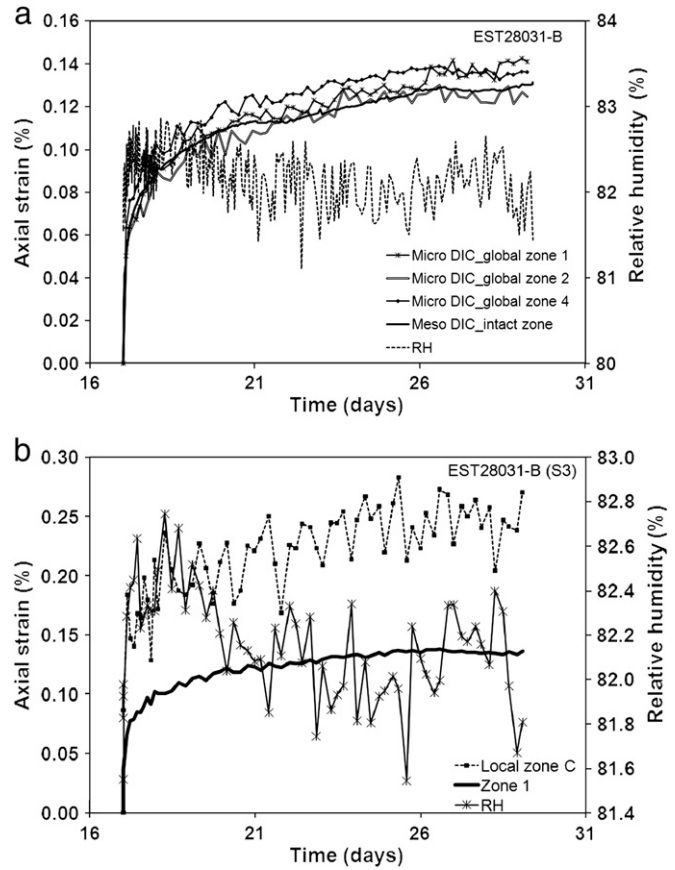


Fig. 8. (a) Axial strain of 4 zones at mesoscopic scale (mm) during the step S4 of EST28031-B; (b) axial strain in the local zone with clay minerals at 100  $\mu\text{m}$  and in the zone 1 (mm) of EST28031-B.

This consistence between the macroscopic scale and mesoscopic scale is not valid when a structural heterogeneity was induced by the propagation of pre-existing cracks or the creation of the new cracks. For instance, the amplitude of the lateral strain rate at the mesoscopic scale ( $4.5 \times 10^{-11} \text{ s}^{-1}$ ) measured by both the MacroDIC and the MicroDIC of EST28031-C in the last creep test at 20 MPa was two orders smaller than that at the macroscopic scale (Fig. 8b). The last creep at macroscale was mainly related to the dilatancy of the sample because of the opening of a macrocrack.

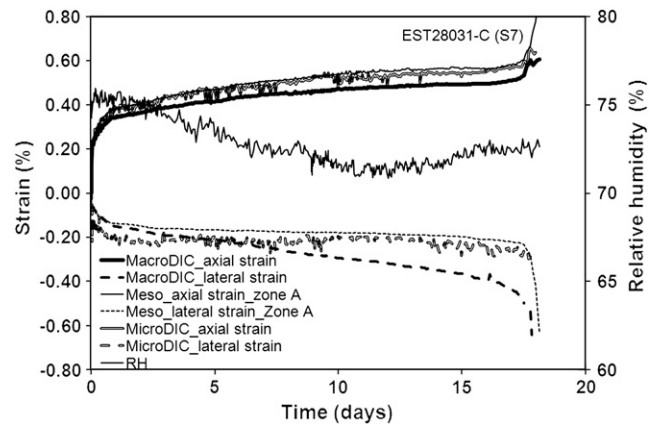


Fig. 9. Strain at various scales (cm and mm) in the last creep step of EST28031-C at 20 MPa under humid condition.

**Table 3**  
Strain rate at mesoscopic scale during the last 4 days of each creep test (EST28031-B).

Local zone (~1 mm)	Grain content (%)	Step	$\epsilon_{axial}$ ( $\times 10^{-11} s^{-1}$ )
Zone 1	29	S3	3.0
Zone 2	37	S3	3.8
		S4	4.4
Zone 3	34	S3	3.6
Zone 4	30	S4	3.3

#### 4.5. Crack effect and the anisotropy

Due to damages created during preparation, swelling and shrinking, several cracks pre-existed in the material. Several pre-existing mesocracks with a length of about a few millimeters (Fig. 3c) were found on the surface after polishing. The cracks normal to the applied stress were closed during the first mechanical loading, and the axial strain in the cracked zone (1.2%) was much larger than in the intact zone (0.2%) (Fig. 10a). Only a small difference was observed between the cracked zone and the intact zone during the steady state creep phase (Fig. 10b). The closure of the crack during mechanical loading and the similar response of the cracked zone relative to that of the intact zone in the steady state are well illustrated on the strain map (Fig. 11a,b).

Some cracks were also found in a direction inclined to the applied stress. For instance, two cracks nearly parallel to the applied stress were identified at the end of the first mechanical loading of EST28031-C (Fig. 12a). These cracks could be pre-existing microcracks created during the sample preparation and could be also related to the contribution of the heterogeneous stress distribution in the sample. Because of their small size ( $<10 \mu m$ ), it was difficult to evaluate the origin of the cracks. These cracks continued to dilate and propagate along the applied stress direction during the creep tests and during

hydration (Fig. 12b,e) and they were completely connected before the sample rupture (Fig. 12f).

The large increase of the lateral strain of EST28031-C was not only related to the cracks, but also related to the swelling of the material during hydration when the relative humidity increased from 25% to 75%. As shown in Fig. 12, the swelling mainly occurred in the clayey matrix, and the strain in the intact zone notably increased. As discussed above (Section 4.2), the amplitude of the lateral strain (0.18%) was larger than that of the axial strain (0.13%) during hydration. It was due to the dilatancy of the material when it reached the moisture equilibrium. As presented in the study of Freissmuth (2002), several cracks at  $\mu m$  scale were found while the relative humidity exceeded 85%. The dilatancy could be related to these cracks.

The ratio between the variations of lateral strain and that of axial strain obtained only during each creep test for EST28031-A and EST28031-B (Fig. 13) becomes greater at higher stresses not only at the macroscopic scale, but also at the microscopic scale. This ratio was considered as an anisotropic parameter and its variation was related to the microstructural changes as shown above during hydration and the creep tests.

## 5. Conclusions

A specific optical setup for uniaxial compression tests was used to investigate the delayed swelling, shrinking, and creep of the argillaceous rocks at various scales (100  $\mu m$ –cm). The results not only revealed the low strain rate at different conditions but also revealed the swelling and shrinking of the material during hydration and dehydration under mechanical loading. The influence of the applied stress on hydration/dehydration was notable. The axial strain of the sample in the uniaxial test was about  $-0.1\%$  during hydration at 1 MPa for the variation of the relative humidity about 10%, but it increased by about 0.83% at 18 MPa when the relative humidity decreased from 75% to 40%.

All the results confirmed that the strain rate increased at higher stress and higher moisture content. The successive creep tests under different moisture contents showed that the strain rate at the same stress (20 MPa) increased by one order of magnitude (from  $1.4 \times 10^{-10} s^{-1}$  to  $1.22 \times 10^{-9} s^{-1}$ ) when the relative humidity increased from 25% to 75%. The cycle of dehydration and rehydration played an important role in the time-dependent deformation and could lead to sample rupture.

The results at the macroscopic scale (cm) were consistent with those at the mesoscopic scale (in 1000  $\mu m$ ) and the heterogeneous response related to the mineralogical composition at these scales, was not significant, but it can be distinguished at 100  $\mu m$ . The delayed behavior of the clay mineral at 100  $\mu m$  was much greater than the zone in millimeter. Because of the sensibility of the clay mineral to the changes in the humidity, it is difficult to determine the creep behavior subjected to the mechanical behavior at 100  $\mu m$  under the actual experimental conditions.

The meso/microcracks played different roles in the time dependent behavior: areas with cracks perpendicular to the applied loads had a strain rate similar to that in intact zones, showing that the axial creep is not related to closing of cracks, in opposition to what can be observed during a stress increase. On the other hand, cracks parallel to the applied stress developed and opened over time and could lead to fracture.

## Acknowledgments

This research was funded by ANDRA and the authors gratefully acknowledge this support. The authors would like to thank the reviewers and the editors for their constructive comments.

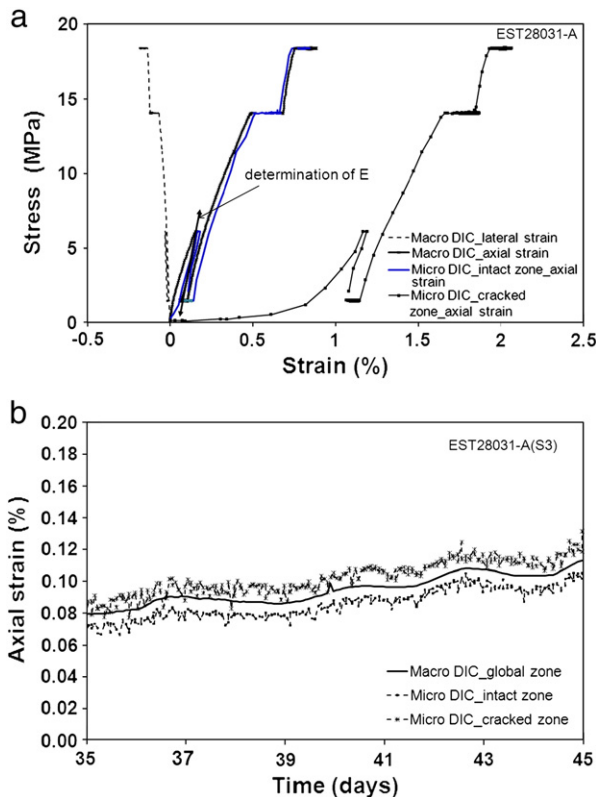


**Fig. 10.** Strain and stress curves (a) and strain at various scales during the second creep test at 18 MPa (b) of EST28031-A.

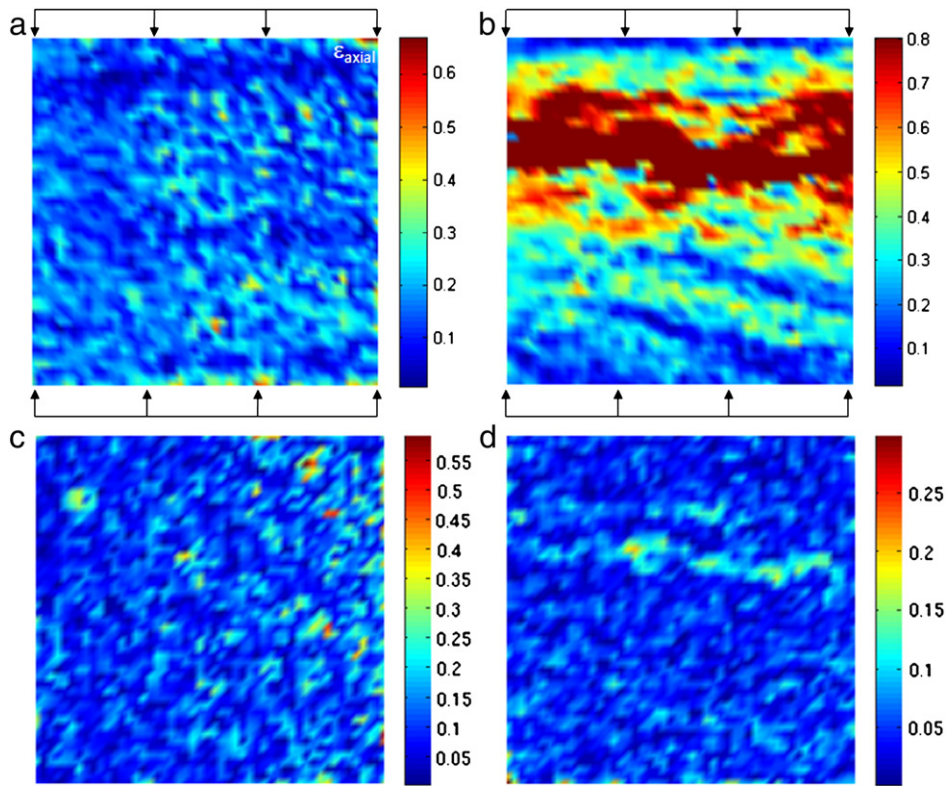


**Fig. 11.** Axial strain map during the mechanical loading (a: 0 MPa to 6 MPa) and during the second creep test at 19 MPa of EST28031-A (b: 26th to 30th day).

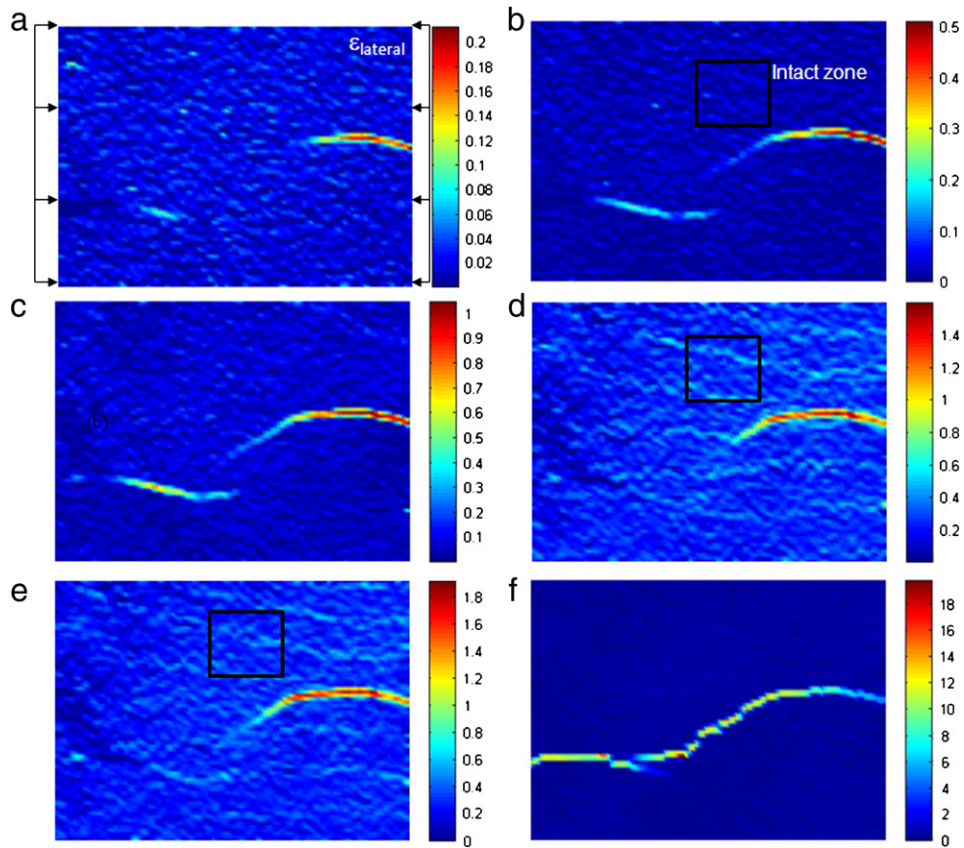


**Fig. 12.** Lateral strain map of EST28031-C: (a)  $\sigma$  from 1 MPa to 10 MPa; (b) end of the 1st creep test at 10 MPa (9th day); (c) end of the 3rd creep test at 20 MPa (41th day); (d) end of the hydration at 10 MPa (69th day); (e) end of the loading from 10 MPa to 20 MPa under RH equal to 75%(70th day); (f) 7th day of the creep test at 20 MPa et under RH equal to 75% (77th day).

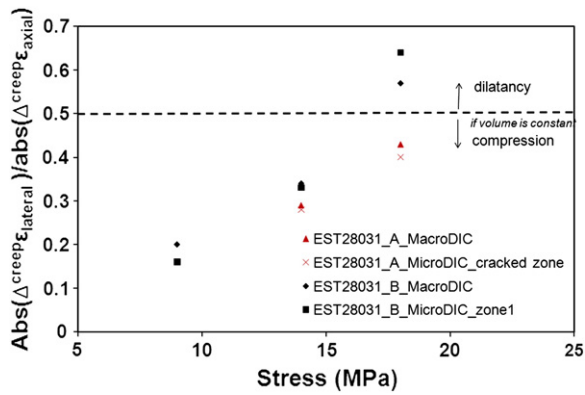


Fig. 13. Ratio between the variation of lateral and axial strain and of axial strain during each creep step.

## References

- Allais, L., Bornert, M., Bretheau, T., Caldemaison, D., 1994. Experimental characterization of the local strain field in a heterogeneous elastoplastic materials. *Acta Metallurgica et Materialia* 42 (11), 3865–3880.
- Bérest, P., 1987. Viscoplasticité en mécanique des roches. In: Darve, F. (Ed.), *Manuel de rhéologie des Géomatériaux*. Presses de l'ENPC, Paris, pp. 235–257.
- Bornert, M., Valès, F., Gharbi, H., Nguyen Minh, D., 2010. Multiscale full-field strain measurements for micromechanical investigations of the hydromechanical behavior of clayey rocks. *Strain* 46, 33–46.
- Chu, T.C., Ranson, W.F., Sutton, M.A., Peters, W.H., 1985. Applications of digital-image-correlation techniques to experimental mechanics. *Experimental Mechanics* 25 (3), 232–244.
- Delage, P., Howat, M.D., Cui, Y.J., 1998. The relationship between suction and swelling properties in a heavily compacted unsaturated clay. *Engineering Geology* 50, 31–48.
- Gasc-Barbier, M., Chanchole, S., Bérest, P., 2004. Creep behavior of Bure clayey rock. *Applied Clay Science* 26, 449–458.
- Fabre, G., Pellet, F., 2006. Creep and time dependent damage in argillaceous rocks. *International Journal of Rock Mechanics and Mining Sciences* 43 (6), 950–960.
- Freissmuth, H., (2002). Influence de l'eau sur le comportement mécanique des roches argileuses. Thèse de doctorat en Technique et Economie de l'Exploitation du Sous-Sol, Ecole Nationale Supérieure des Mines de Paris, 122 p.
- Jia, Y., Bian, H.B., Su, K., Kondo, D., Shao, J.F., 2010. Elastoplastic damage modeling of desaturation and resaturation in argillites. *International Journal for Numerical and Analytical Methods in Geomechanics* 34 (2), 187–220.
- Niandou, H., Shao, J.F., Henry, J.P., Fourmaintraux, D., 1997. Laboratory investigation of the mechanical behaviour of Tournemire shale. *International Journal of Rock Mechanics and Mining Sciences* 34, 3–16.
- Pham, Q.T., Valès, F., Malinsky, L., Nguyen, Minh D., Gharbi, H., 2007. Effets of desaturation-resaturation on mudstone. *Physics and Chemistry of the Earth* 32, 646–655.
- Pusch, R., 1993. Mechanisms and consequences of creep in crystalline rocks. In: Hudson, J.A. (Ed.), *Comprehensive Rock Engineering (Principles, Practices, Projects): Fundamentals*, vol. 1. Pergamon, Oxford, pp. 227–241.
- Sayers, C.M., 1994. The elastic anisotropy of shales. *Journal of Geophysical Research* 99, 767–774.
- Shao, J.F., Zhu, Q.Z., Su, K., 2003. Modeling of creep in rock materials in terms of material degradation. *Computers and Geotechnics* 30, 549–555.
- Sutton, M.A., Wolters, W.J., Peters, W.H., Ranson, W.F., McNeil, S.R., 1983. Determination of displacements using an improved digital correlation method. *Image and Vision Computing* 1 (3), 133–139.
- Sutton, M.A., Orteu, J.J., Schreier, H.W., 2009. *Image Correlation for Shape, Motion and Deformation Measurements: Basic Concepts, Theory and Applications*. Springer, 316p.
- Valès, F., Nguyen, Minh D., Gharbi, H., Rejeb, A., 2004. Experimental study of the influence of the degree of saturation on physical and mechanical properties in Tournemire argillite (France). *Applied Clay Science* 26, 197–207.
- Valès, F., (2008). Modes de déformation et d'endommagement de roches argileuses profondes sous sollicitations hydro-mécaniques. PhD dissertation, Ecole Polytechnique, 356p.
- Wright, H. (2001) Rôle de la minéralogie, de la texture et de la structure dans la déformation et la rupture des argilites de l'Est. Thèse de Doctorat en Sciences, Paris, 210p.
- Yang, D.S., Billiotte, J., Su, K., 2010a. Characterization of the hydromechanical behavior of argillaceous rocks with effective gas permeability under deviatoric stress. *Engineering Geology* 114 (3–4), 116–122.
- Yang, D.S., Bornert, M., et al., 2010b. Optimized optical setup for DIC in rock mechanics. *The European Physical Journal* 6. doi:10.1051/epjconf/20100622019.
- Zhang, C.L., Rothfuchs, T., Su, K., Hoteit, N., 2007. Experimental study of the thermohydro-mechanical behavior of indurated clays. *Physics and Chemistry of the Earth* 32, 957–965.